Nano Research
2024, 17(7): 6575–6581

ISSN 1998-0124 CN 11-5974/O4
https://doi.org/10.1007/s12274-024-6576-7

Research Article

Gate-controlled supercurrent effect in dry-etched Dayem bridges of non-centrosymmetric niobium rhenium

Jennifer Koch[1], Carla Cirillo[2], Sebastiano Battisti[3], Leon Ruf[1], Zahra Makhdoumi Kakhaki[4], Alessandro Paghi[3], Armen Gulian[5], Serafim Teknowijoyo[5], Giorgio De Simoni[3], Francesco Giazotto[3], Carmine Attanasio[4], Elke Scheer[1] (✉), and Angelo Di Bernardo[1,4] (✉)

[1] *Department of Physics, University of Konstanz, Universitätsstraße 10, 78464 Konstanz, Germany*
[2] *CNR-Spin, c/o Università degli Studi di Salerno, via Giovanni Paolo II 132, 84084 Fisciano (SA), Italy*
[3] *NEST, Istituto Nanoscienze-CNR and Scuola Normale Superiore, Piazza San Silvestro 12, 56127 Pisa, Italy*
[4] *Dipartimento di Fisica "E. R. Caianiello", Università degli Studi di Salerno, Via Giovanni Paolo II 132, 84084 Fisciano (SA), Italy*
[5] *Advanced Physics Laboratory, Institute for Quantum Studies, Chapman University, Burtonsville, MD 20866, USA*

© The Author(s) 2024

Received: 16 December 2023 / **Revised:** 8 February 2024 / **Accepted:** 19 February 2024

ABSTRACT

The application of a gate voltage to control the superconducting current flowing through a nanoscale superconducting constriction, named as gate-controlled supercurrent (GCS), has raised great interest for fundamental and technological reasons. To gain a deeper understanding of this effect and develop superconducting technologies based on it, the material and physical parameters crucial for the GCS effect must be identified. Top-down fabrication protocols should also be optimized to increase device scalability, although studies suggest that top-down fabricated devices are more resilient to show a GCS. Here, we investigate gated superconducting nanobridges made with a top-down fabrication process from thin films of the non-centrosymmetric superconductor niobium rhenium with varying ratios of the constituents (NbRe). Unlike other devices previously reported and made with a top-down approach, our NbRe devices systematically exhibit a GCS effect when they were fabricated from NbRe thin films with small grain size and etched in specific conditions. These observations pave the way for the realization of top-down-made GCS devices with high scalability. Our results also imply that physical parameters like structural disorder and surface physical properties of the nanobridges, which can be in turn modified by the fabrication process, are crucial for a GCS observation, providing therefore also important insights into the physics underlying the GCS effect.

KEYWORDS

superconductivity, non-centrosymmetric superconductors, superconducting devices, gated devices, gate-controlled supercurrent, top-down fabrication

1 Introduction

The recent discovery [1] that the superconducting critical current (I_c) of a nanoconstriction made from a superconductor (S) can be controlled via a gate voltage (V_G) has raised great interest for both fundamental and technological reasons. These reasons have motivated studies on a variety of gated superconducting devices, made with different Ss, geometries, and fabrication processes [1–24], to determine under which conditions an applied V_G can switch a S nanoconstriction from a superconducting state (with $I_c \neq 0$) to a resistive state (with $I_c = 0$). Although a V_G-driven modulation of the I_c, currently referred to as gate-controlled supercurrent (GCS) [22–25], has been observed in these studies [1–24], the mechanism underlying GCS as well as the microscopic parameters and physical properties crucial for its observation remain not fully understood [25].

To date, several mechanisms have been proposed to explain GCS, which have been recently classified into four categories [25]. These categories include tunnelling of electrons [26] between the gate and S nanoconstriction across vacuum (scenario 1) [13–15], heating induced by phonons triggered by the leakage current (I_{leak}) flowing from the gate into the S nanoconstriction (scenario 2) [13, 16, 21], I_{leak}-induced phase fluctuations but without sizable heating (scenario 3) [16, 17, 20, 22 23], and microscopic mechanisms driven by the electric field associated to V_G (scenario 4) [1–12, 18, 23, 24, 27–30].

Although some of these mechanisms (e.g., scenarios 1 and 2) may be at play in specific devices (e.g., devices made on Si substrates) [25], no conclusive experiments have been reported that fully rule out the other two mechanisms (scenarios 3 and 4) and/or exactly quantify their relative contributions to the GCS.

Understanding the mechanisms behind a GCS is not only a fundamental challenge, but may also prove crucial to enhance the performance of GCS-based devices. Figures of merit of such devices include the operational speed and the V_G needed for a full I_c suppression ($V_{G,offset}$).

While speed may be limited in case of considerable heat dissipation (scenarios 1 and 2), GCS devices based on mechanism 3 or 4 may compete, in terms of speed, with existing superconducting logics [31, 32].

Address correspondence to Elke Scheer, elke.scheer@uni-konstanz.de; Angelo Di Bernardo, angelo.dibernardo@uni-konstanz.de

清華大学出版社 Tsinghua University Press Springer

Reducing $V_{G,offset}$ (typically of few tens of Volts) is also necessary from a technological point of view to interconnect GCS-based devices in series. This is because, once a device is driven into its resistive state by an applied $V_G > V_{G,offset}$, its output voltage (V_{out}) can be used to control an adjacent GCS-based device if $V_{out} \geq V_{G,offset}$ also for the latter device. A similar argument can be made regarding the interfacing of GCS-based logics to complementary metal-oxide semiconductor (CMOS) circuits working at voltages < 5 V [33, 25].

Another major challenge for applications is to achieve good reproducibility and scalability in GCS-based devices. To increase reproducibility, understanding the mechanism and the parameters behind GCS is crucial. For high scalability, top-down fabrication protocols based on subtractive patterning compatible with CMOS fabrication [34] as well as with fabrication of S-based qubit platforms [35] are preferable.

In a recent study [23], it has been shown that top-down-fabricated devices from Ss like Nb or NbTiN do not systematically exhibit GCS, unlike those made following a bottom-up approach (i.e., via additive patterning). This observation has been ascribed to differences in the microstructural properties of the S nanoconstrictions, which have a rougher interface with the substrate and a more disordered surface in devices made with a bottom-up approach [23].

To investigate whether specific microstructural parameters and surface properties promote the GCS also in devices made with a top-down approach, in this work we study gated superconducting devices made by subtractive patterning from thin films of niobium rhenium with different compositions (NbRe), for which GCS has not been yet explored. We have chosen NbRe as our S material because the results reported in Ref. [23] suggest that disorder is an important parameter to observe a GCS, depending on the way they are fabricated, NbRe thin films can be strongly disordered [36].

We also note that NbRe has other physical properties like high spin-orbit coupling (SOC), which may be relevant for the GCS effect [25], and a non-centrosymmetric crystal structure with an unconventional superconducting order parameter, at least in bulk single-crystal form [37, 38].

We find that our NbRe devices can exhibit GCS, even though they were made using a top-down fabrication protocol, under certain conditions: they need to be patterned from strongly disordered films and a specific gas mixture (consisting of Ar and Cl_2) has to be used for the etching process. The GCS effect is instead systematically absent in our devices etched from polycrystalline NbRe thin films (with larger grain size) or those etched from disordered NbRe thin films but with different gas mixtures, even in the presence of a significant I_{leak} (> 10 nA).

Last, in our NbRe devices showing GCS, the distance between the gate and the S nanoconstriction (d_g) is up to 300 nm, and therefore larger than the d_g typically reported (< 100 nm) to observe a GCS effect [1, 8, 9, 14, 15], which shows that NbRe-based GCS devices are not very demanding from a fabrication-related point of view.

2 Experimental

2.1 Thin film growth and characterization

Our gated NbRe devices were fabricated from thin films using a top-down fabrication process. For all devices reported in this study (10 in total identified with labels from D1 to D10), films of two different compositions and thicknesses were used, specifically 20-nm-thick $Nb_{0.18}Re_{0.82}$ (devices from D1 to D7) and 30-nm-thick $Nb_{0.10}Re_{0.90}$ (devices from D8 to D10). All films were deposited on Al_2O_3 substrates.

Structural characterization of the thin films based on X-ray diffraction (XRD) and reported in Fig. S1 in the Electronic Supplementary Material (ESM) shows that the $Nb_{0.18}Re_{0.82}$ thin films were strongly disordered (either polycrystalline with very small grain size of 1–2 nm or even amorphous), as reported in Ref. [39], whilst $Nb_{0.10}Re_{0.90}$ thin films were polycrystalline with grain sizes (~ 28 nm deduced from the (330) peak and Scherrer's formula [40]) comparable to the film thickness (~ 30 nm).

The difference in the grain size and structural disorder for the two types of films is due to their different growth conditions. In particular, $Nb_{0.10}Re_{0.90}$ thin films were *in-situ* annealed at high temperature after growth, which was most likely the reason for their larger grain size and polycrystalline structure, whilst $Nb_{0.18}Re_{0.82}$ thin films were grown at room temperature, as further discussed below.

The NbRe thin films with composition $Nb_{0.18}Re_{0.82}$ were deposited by direct current (DC) magnetron sputtering onto a plane Al_2O_3 (sapphire) substrates inside an ultra-high vacuum (UHV) chamber, with a base pressure of 2×10^{-8} Torr. A stoichiometric target (99.95% purity) mounted on a 2" circular gun was used for the growth process, which was ignited with a power of 250 W in an Ar pressure of 3 mTorr. This resulted in a sputtering rate of 0.33 nm/s [39] measured with a quartz crystal monitor previously calibrated based on thickness measurements of test films made with a profilometer.

The Nb and Re concentrations in these thin films were confirmed using energy dispersive X-ray (EDX) analysis, as shown in Fig. S2 in the ESM. In addition, transmission electron microscopy (TEM) characterization of thin films grown in the same conditions showed that such films were completely homogeneous, without any dispersed Nb or Re islands [36]. More details about the fabrication of these thin films can be found in Ref. [36].

After deposition, the $Nb_{0.18}Re_{0.82}$ films were capped with a polymethyl methacrylate (PMMA) protection layer.

The $Nb_{0.10}Re_{0.90}$ thin films were also prepared by DC magnetron in a UHV chamber at a base pressure of 10^{-8} Torr, but using co-sputtering from two elemental targets (1.5" diameter each, Re 99.99% purity and Nb 99.95% purity) and their composition was also confirmed by EDX (Fig. S3 in the ESM). The Al_2O_3 substrate (thickness 650 μm, c-plane) used for the thin film growth was cleaned thoroughly with isopropyl alcohol before being mounted on the sample holder. Before growth, an additional *in-situ* cleaning of the substrate was also carried out, which involved first heating the substrate up to 700 °C and then cleaning its surface using a Kauffman source with Ar^+ at a pressure of 0.75 mTorr for 5 min at 600 °C. The Nb and Re targets were both ignited at 30 mTorr with the shutter closed using an initial power of 30 W for each of them. Right before the material deposition, the power of the magnetron guns was ramped up to 150 W for Nb and up to 500 W for Re, whilst the Ar chamber pressure was reduced to 5 mTorr. During the deposition, the Re shutter was opened 10 s later than the Nb shutter to achieve better adhesion to the substrate. Nb and Re were then co-sputtered for 150 s, after which the Re shutter was closed first followed by the Nb shutter after 10 s. After the deposition, the temperature of the substrate holder was raised to 900 °C for *in-situ* annealing, which was carried out for 30 min before cooling the samples down to room temperature with a ramp rate of 30 °C/min (this rate was also used for all the other heating steps).

2.2 Device fabrication with top-down protocols

The $Nb_{0.18}Re_{0.82}$ and $Nb_{0.10}Re_{0.90}$ films were patterned into devices using e-beam lithography (EBL) to define the device geometry and dry-etched using a negative resist and Al hard mask, respectively.

For the devices made from $Nb_{0.18}Re_{0.82}$ thin films, after removing the protective PMMA layer in acetone, a 200-nm-thick layer of negative resist was spun onto the NbRe thin film for pattern transfer by EBL with a dose between 60 and 70 μC/cm^2. After the exposure, the samples were developed, which left a resist mask for dry plasma etching.

The reactive ion etching (RIE) was carried out using three different systems (RIE I, RIE II, and RIE III), which were varied across devices as indicated in the main text and specified in Table S1 in the ESM. RIE I and II used inductively coupled plasma (ICP) sources but with different powers and gas mixtures; RIE III was equipped with a standard radio frequency (RF) source. For devices etched in RIE I (from D1 to D3), a mixture of 26 sccm of Ar and 26 sccm of Cl_2 with a total pressure of 10 mTorr was used. The power in this system was set as a combination of ICP power (750 W) and RIE power (20 W), resulting in a total etching time of 30 s to obtain the desired nanoscale devices. The same process was also followed to etch device D10 made from $Nb_{0.10}Re_{0.90}$ thin films with an increased etching time of ~ 180 s, possibly because the film was harder to etch due to the larger size of its grains.

Samples from D4 to D7 were etched in the RIE II. Device D4 was etched with 26 sccm Ar with a pressure of 10 mTorr at an RIE power of 50 W and an ICP power of 100 W for 5 min and 30 s. For device D5, the powers were changed to an RIE power of 200 W and an ICP power of 50 W (in order to achieve a more anisotropic etching), resulting in a total etching time of 2 min 30 s. For the devices D6 and D7, a mixture of 26 sccm Ar and 26 sccm SF_6 at a pressure of 10 mTorr was used in combination with an RIE power of 200 W and an ICP power of 50 W, resulting in an etching time of 30 s.

Whilst etching all devices from D1 to D7, the sample plate was cooled down to 10 °C and kept at this temperature during the etching process to avoid a collapse of the resist mask.

To pattern devices D8 and D9, a positive EBL polymer layer of PMMA was first spun onto the thin films. After carving the device geometry into the resist layer by EBL, a 60-nm-thick Al layer was deposited with an e-beam evaporator. The evaporated Al was used as a hard mask for the etching process, since Al had a good resistance against fluorine. The NbRe thin films were hence etched in RIE III using a $CF_4/Ar/O_2$ gas mixture of 40/6/4 sccm, respectively, at a power of 150 W, after which the Al hard mask was removed with an alkaline solution before device testing.

3 Results and discussion

3.1 Superconducting properties of NbRe devices

As discussed in Section 2, across our devices, we changed the gas mixture used for the etching process (Table S1 in the ESM), which we find to be the most crucial parameter for the GCS observation, together with the degree of crystallinity of the starting NbRe thin film.

Since we followed a top-down fabrication process involving an etching step for the fabrication of all devices, in the following we refer to them as etched devices.

All our etched NbRe devices were fabricated with a Dayem bridge geometry consisting of two large electrodes separated by a narrow constriction (bridge) [41], as shown in Fig. 1(a). The width of the bridge ranges between 50 and 350 nm, whilst the length is between 175 and 220 nm. In our devices, d_g varies between 50 and 300 nm, with the gate electrode always placed only on one side of the S nanoconstriction (Fig. 1(b)).

Figure 1 shows the resistance versus temperature, $R(T)$, for device D1, which has a superconducting critical temperature (T_c) of ~ 6.1 K and a normal-state resistance (R_N) of ~ 1.1 kΩ. We define T_c as the temperature (T) at which R reaches 50% of R_N at 10 K (Fig. 1(c)). For comparison, the 20-nm-thick film used for the fabrication of this device has T_c of ~ 6.7 K before patterning [39]. This suggests that our fabrication process in combination with the short superconducting coherence length ξ of NbRe (~ 5 nm; Refs. [39, 42]) preserves good superconducting properties in our Dayem bridges.

3.2 Observation of the GCS effect in etched NbRe devices

For all our devices, we measured the evolution of I_c, extracted from current versus voltage $I(V)$ characteristics under an applied V_G (Fig. 2(a)). Our results discussed below suggest that only devices dry-etched from disordered $Nb_{0.18}Re_{0.82}$ thin films using an Ar/Cl_2 gas mixture (from D1 to D3) show a GCS, whilst devices dry-etched with different gas mixtures (from D4 to D9) or also with an Ar/Cl_2 mixture but starting from polycrystalline $Nb_{0.10}Re_{0.90}$ thin films (D10) show no GCS, even in the presence of a larger I_{leak} and smaller d_g compared to devices with a GCS. We also observed a significant variation in the behaviour of the devices showing a GCS, suggesting that different mechanisms may be at play across these devices (see below).

The evolution of the $I_c(V_G)$ curves in an applied out-of-plane magnetic field B_{ext} (Fig. S4(b) in the ESM) also confirms that the GCS effect persists until B_{ext} suppresses superconductivity, consistent with previous studies [1, 5, 16].

The observation of GCS in device D1 and other devices (D2 and D3; see below) is remarkable for two reasons. First, d_g for these devices is three times larger than the typical d_g (< 100 nm) in which a GCS was reported so far [25]. This also suggests that a d_g reduction may lead to an additional reduction in $V_{G,offset}$. Second, it has been reported that etched devices made of Ss different from NbRe (e.g., Nb or NbTiN) do not show a GCS [23]. The GCS effect is also absent in devices fabricated following our route (i.e.,

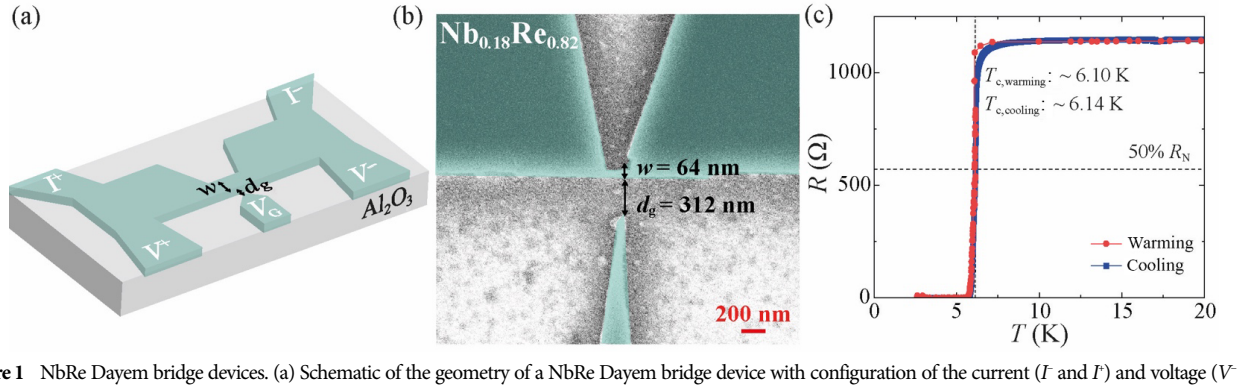

Figure 1 NbRe Dayem bridge devices. (a) Schematic of the geometry of a NbRe Dayem bridge device with configuration of the current (I^- and I^+) and voltage (V^- and V^+) pads and of the V_G, with false-colour scanning electron micrograph of a device (device D1) fabricated based on this layout in (b). (c) Resistance versus temperature $R(T)$ curve of the NbRe device D1 in (b) measured near its superconducting transition in both cooling (blue curve) and warming (red curve).

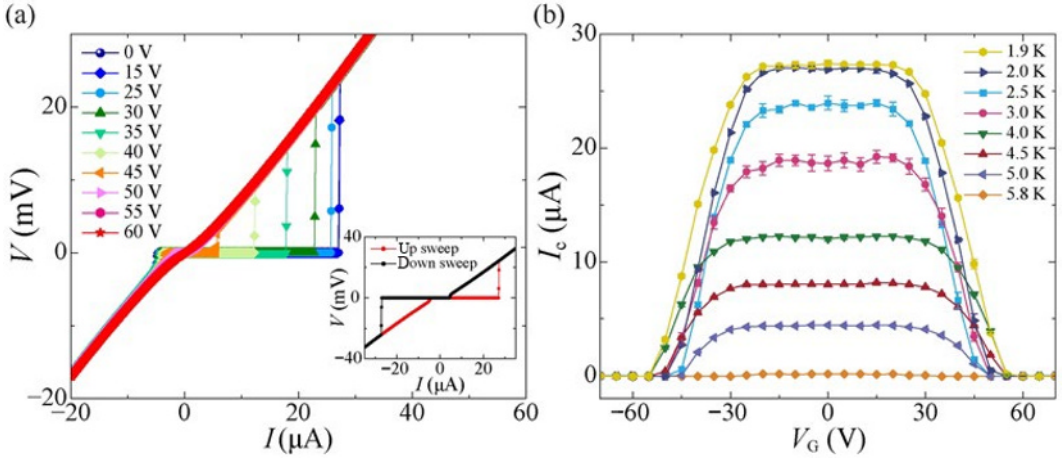

Figure 2 Gate-controlled supercurrent in NbRe device D1. (a) $I(V)$ characteristics measured at T = 2.0 K for a NbRe Dayem bridge (device D1) at different applied V_G values (specified in the panel legend). The $I(V)$ curves shown in the main panel are measured whilst sweeping I from negative to positive values (up-sweeping). The inset shows the $I(V)$ characteristic measured at the same T = 2.0 K and at V_G = 0 whilst up-sweeping (red curve) and down-sweeping (black curve) the bias current I. (b) $I_c(V_G)$ curves measured for the same device as in (a) at different Ts (specified in the panel legend).

with the same Ar/Cl_2 gas mixture) but using other Ss other than strongly-disordered NbRe thin films [23].

Figure 2(b) shows the $I_c(V_G)$ characteristics measured at different Ts from 1.9 to 5.8 K below T_c (~ 6.1 K) for device D1, which reveals a GCS with $V_{G,offset}$ of ~ 55 V. As suggested in Ref. [25], we define $V_{G,offset}$ as the point where the linear part of the $I_c(V_G)$ curve (i.e., the curve section where I_c decays) intercepts the horizontal axis at I_c = 0. We also define $V_{G,onset}$ as the V_G value of the $I_c(V_G)$ characteristic corresponding to a 10% drop in the I_c measured at V_G = 0 [25]. Compared with other devices reported in the literature and mostly made of elemental Ss (e.g., Nb, Al, and Ti), for which $V_{G,offset}$ varies between 10 and 40 V [7, 9, 10], $V_{G,offset}$ measured for D1 is relatively large (~ 55 V).

Other possible reasons why etched devices from disordered NbRe show a GCS, unlike the devices reported in Ref. [23], may be related to different physical properties of the Ss used. First, unlike Nb or NbTiN, NbRe is a non-centrosymmetric S. The non-centrosymmetric structure is also linked to strong SOC and to an unconventional superconducting order parameter [37, 38]. Although we cannot quantify the role of these two physical properties on GCS—comprehensive theoretical investigations would be needed—our $Nb_{0.18}Re_{0.82}$ films are more disordered [35, 39] than the NbTiN and Nb thin films used in Ref. [23]. The high disorder is not only evident from the grain size (1–2 nm) being much smaller than the film thickness [35], but also from their low-T electronic transport properties. Indeed, the films used for the devices with GCS (from D1 to D3) have a residual resistivity ratio (RRR) below 1 (Fig. S2 in the ESM) [35–37], and their T_c increases as their resistivity ρ gets larger (up to ρ of ~ 100 μΩ·cm for a thickness of 20 nm [35]), which are typical signatures of strong disorder in S thin films [43, 44].

The films with composition $Nb_{0.10}Re_{0.9}$ used for devices D8 to D10 are polycrystalline and show no GCS. This observation demonstrates that small grain size (smaller than the film thickness) is crucial to observe a GCS in our etched NbRe devices.

3.3 Variations in GCS across NbRe devices

Across the NbRe devices showing GCS (D1 to D3), we observe a different T-dependence of $V_{G,offset}$ and of I_{leak}, from which we infer that the GCS is dominated by different physical mechanisms in these devices. We note that all three devices have been fabricated within the same batch, meaning from $Nb_{0.18}Re_{0.82}$ thin films grown together and then processed (for EBL, etching, etc.) also together. Therefore, variations in the material or fabrication process for these devices should be negligible.

In Fig. S4 of the ESM, we report the I_{leak} versus V_G, $I_{leak}(V_G)$, characteristics for device D1 measured at the same Ts of the $I_c(V_G)$ curves in Fig. 2(b). At $V_{G,onset}$ of ~ 24 V, I_{leak} is ~ 100 pA and is almost independent of T. On the other hand, I_{leak} measured at $V_{G,offset}$ for the same device shows a strong T-variation, although I_{leak} does not increase monotonically with increasing T. $V_{G,offset}$ also shows a similar T-dependence (see Fig. 2(b)).

For the other two devices with GCS (D2 and D3), $V_{G,offset}$ is of the same order of magnitude (~ 65 V) as for device D1. For D2, however, $V_{G,offset}$ gets reduced monotonically, and simultaneously I_{leak} (at $V_{G,offset}$) gets smaller as T is increased (Fig. S6 in the ESM). In device D2 therefore, GCS is mostly induced by I_{leak} because, as T is increased and superconductivity gets weaker, a lower I_{leak} is measured whilst the device is driven into the normal state by V_G.

The $I_c(V_G)$ curves for device D3 in Fig. 3(a) show that $V_{G,onset}$ of ~ 40.8 V and $V_{G,offset}$ of ~ 64 V are almost unaffected by T, which are opposite to what measured for device D2. The I_{leak} values measured at $V_{G,onset}$ and $V_{G,offset}$ are also T-independent and equal to 0.2 and 3 nA, respectively.

The different behaviours of the devices from D1 to D3 are also shown in Fig. 4, where we plot $V_{G,offset}$ as a function of T for all three devices. The strong decrease of $V_{G,offset}$ with T for device D2 again suggests that I_{leak}-induced Joule heating (scenario 2 above) may be the main mechanism responsible for the GCS effect in device D2.

To estimate the role of Joule heating in devices D1 and D3, we compare the power dissipated by the gate $P_G = V_G \times I_{leak}$, with the power dissipated by Joule heating when the device switches to the resistive state, which we estimate as $P_N = R_N \times I_r^2$ (I_r being the retrapping current).

For device D3, for example, at T = 2.0 K, P_G is ~ 8.2 nW at $V_{G,onset}$, where it is already comparable to P_N of ~ 16 nW (R_N = 1.264 kΩ and I_r = 3.54 μA at V_G = 0). This may suggest that Joule heating is the main contribution to the GCS also for device D3.

Nonetheless, the I_{leak} indicated for our devices (Fig. 3, and Figs. S4 and S6 in the ESM) and used to calculate P_G does not correspond just to the I_{leak} flowing through the S nanoconstriction, but it also includes contributions from the cryostat wiring. In our setup, V_G is applied to the impedances of the gate electrode and of the setup cabling, which are connected in series between the V_G generator and the setup electrical ground. As a result, we overestimated the actual P_G dissipated by the Dayem bridge. To confirm this, we have also placed a reference resistor (R_{ref}) in series between the gate electrode and ground, to determine the actual I_{leak} flowing across the bridge, based on the measurement of the

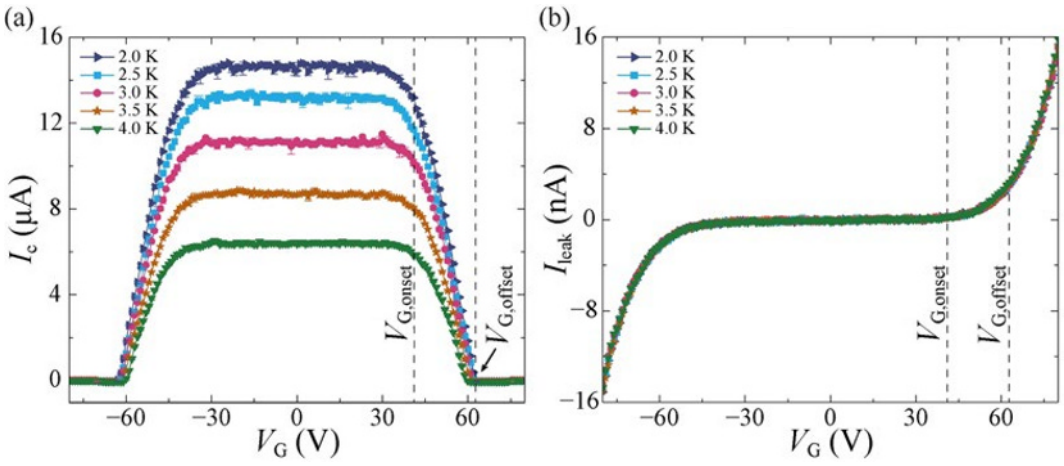

Figure 3 Gate-controlled supercurrent effect in NbRe device D3. (a) $I_c(V_G)$ curves measured for a NbRe Dayem bridge (device D3) at different *T*s (specified in the panel legend) with corresponding $I_{leak}(V_G)$ curves at the same *T*s in (b).

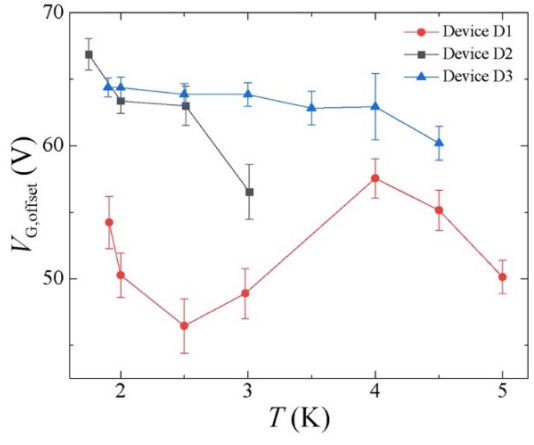

Figure 4 Comparison of etched NbRe device. $V_{G,offset}(T)$ curves for devices from D1 to D3 made by etching in an Ar/Cl_2 gas mixture.

voltage across R_{ref}. For this configuration, which we have tested on twin devices to devices from D1 to D3, we find I_{leak} values lower by one order of magnitude than those measured for the total I_{leak}.

We are therefore confident that the actual P_G dissipated within the NbRe bridges of devices from D1 to D3 is lower than that calculated from the measured I_{leak} by at least one order of magnitude. This estimation and the *T*-independent behaviour of $V_{G,offset}$, consistent with other reports where Joule heating has been ruled out [1, 13, 22], suggest that different mechanisms are at play in devices D1 and D3 (compared to device D2).

3.4 Key parameters for GCS in NbRe devices

Another main result of our work is that, in addition to a high structural disorder, the etching process, specifically the gas mixture used, is crucial for the GCS observation. As reported in Table S1 in the ESM, in addition to devices etched in an Ar/Cl_2 mixture (D1 to D3), we have also made devices from the same disordered $Nb_{0.18}Re_{0.82}$ thin films, but using Ar gas only (D4 and D5) or Ar/SF_6 mixtures (D6 and D7). Nonetheless, none of the etched devices shows a GCS up to V_G of ~ 100 V (Fig. S7 in the ESM), although some have a smaller d_g (~ 90 nm) and larger I_{leak} compared to devices D1 or D3. This also suggests that, although I_{leak} can play a role towards GCS, a large I_{leak} *per se* is not sufficient to observe GCS in our etched NbRe devices.

Since Ar/Cl_2 [23] has also been used to etch devices made of other Ss (e.g., Nb) and these devices showed no GCS, we conclude that this provides additional evidence that the intrinsic high disorder of some of our NbRe films in combination with their surface properties, possibly activated by the etching gas, are key for the GCS observation.

Although the high structural disorder in our NbRe can assist a GCS, disorder alone is not sufficient for GCS because devices etched with Ar or Ar/SF_6 show no GCS, as discussed above. The strong correlation between a GCS and the etchant gas suggests that surface chemistry is also crucial.

It has been shown that the reaction of Cl_2 with Re results in the formation of $ReCl_5$ and other Re halides [45, 46] with magnetic properties [47, 48]. Since a GCS is only observed in NbRe devices etched with Ar/Cl_2, these Re-based magnetic species forming on the surface may assist a GCS , consistent with a recent theoretical proposal [30]. Future studies on etched devices made from Re thin films may further validate this argument.

4 Conclusions

In summary, we have shown that structural disorder combined with surface properties, and how these are modified by the fabrication process, can lead to a systematic GCS effect in etched NbRe devices.

We also note that we observe a GCS despite an unusually large d_g (~ 300 nm), for which a GCS is not observed in devices made of other Ss [25]. This may suggest that other physical properties (e.g., large SOC, unconventional order parameter) can further assist the GCS effect in NbRe devices with the right structural disorder and surface properties.

Although an I_{leak}-induced mechanism can account for the GCS effect observed in our NbRe devices, our results show that this mechanism still has to find a S nanoconstriction with a suitable combination of surface and microstructural properties, to trigger a GCS.

Our study identifies a set of parameters that might be subject of further investigation, also of theoretical nature, aiming at understanding their role on the GCS effect. We also define a fabrication protocol that can be tested on other Ss similar to NbRe and represents a first step towards achieving high reproducibility and scalability in GCS-based devices made with a top-down approach.

Acknowledgements

The authors acknowledge support from the European Union's Horizon 2020 Research and Innovation Program under Grant Agreement No. 964398 (SuperGate). A. G. and S. T. also acknowledge support from the US ONR (Nos. N00014-21-1-2879, N00014-20-1-2442, and N00014-23-1-2866).

Funding note: Open Access funding enabled and organized by Projekt DEAL.

Electronic Supplementary Material: Supplementary material ($I_{leak}(V_G)$ curves at different temperature and $I_c(V_G)$ curves at different B_{ext} for device D1, $R(T)$ curve for $Nb_{0.18}Re_{0.82}$ thin film from room temperature down to low temperature, $I_c(V_G)$ and $I_{leak}(V_G)$ curves at different temperature for device D2, $I_c(V_G)$ curves at two different temperatures for device D6, and additional data on geometry and etching parameters for all devices) is available in the online version of this article at https://doi.org/10.1007/s12274-024-6576-7.

Open Access This article is licensed under a Creative Commons Attribution 4.0 International License, which permits use, sharing, adaptation, distribution and reproduction in any medium or format, as long as you give appropriate credit to the original author(s) and the source, provide a link to the Creative Commons licence, and indicate if changes were made.

The images or other third party material in this article are included in the article's Creative Commons licence, unless indicated otherwise in a credit line to the material. If material is not included in the article's Creative Commons licence and your intended use is not permitted by statutory regulation or exceeds the permitted use, you will need to obtain permission directly from the copyright holder.

To view a copy of this licence, visit http://creativecommons.org/licenses/by/4.0/.

References

[1] De Simoni, G.; Paolucci, F.; Solinas, P.; Strambini, E.; Giazotto, F. Metallic supercurrent field-effect transistor. *Nat. Nanotechnol.* **2018**, *13*, 802–805.

[2] De Simoni, G.; Paolucci, F.; Puglia, C.; Giazotto, F. Josephson field-effect transistors based on all-metallic Al/Cu/Al proximity nanojunctions. *ACS Nano* **2019**, *13*, 7871–7876.

[3] Paolucci, F.; Vischi, F.; De Simoni, G.; Guarcello, C.; Solinas, P.; Giazotto, F. Field-effect controllable metallic Josephson interferometer. *Nano Lett.* **2019**, *19*, 6263–6269.

[4] Paolucci, F.; De Simoni, G.; Solinas, P.; Strambini, E.; Ligato, N.; Virtanen, P.; Braggio, A.; Giazotto, F. Magnetotransport experiments on fully metallic superconducting Dayem-bridge field-effect transistors. *Phys. Rev. Appl.* **2019**, *11*, 024061.

[5] Paolucci, F.; De Simoni, G.; Solinas, P.; Strambini, E.; Puglia, C.; Ligato, N.; Giazotto, F. Field-effect control of metallic superconducting systems. *AVS Quantum Sci.* **2019**, *1*, 016501.

[6] De Simoni, G.; Puglia, C.; Giazotto, F. Niobium Dayem nano-bridge Josephson gate-controlled transistors. *Appl. Phys. Lett.* **2020**, *116*, 242601.

[7] Bours, L.; Mercaldo, M. T.; Cuoco, M.; Strambini, E.; Giazotto F. Unveiling mechanisms of electric field effects on superconductors by a magnetic field response. *Phys. Rev. Res.* **2020**, *2*, 033353.

[8] Puglia, C.; De Simoni, G.; Ligato, N.; Giazotto, F. Vanadium gate-controlled Josephson half-wave nanorectifier. *Appl. Phys. Lett.* **2020**, *116*, 252601.

[9] Puglia, C.; De Simoni, G.; Giazotto, F. Electrostatic control of phase slips in Ti Josephson nanotransistors. *Phys. Rev. Appl.* **2020**, *13*, 054026.

[10] Rocci, M.; De Simoni, G.; Puglia, C.; Degli Esposti, D.; Strambini, E.; Zannier, V.; Sorba, L.; Giazotto, F. Gate-controlled suspended titanium nanobridge supercurrent transistor. *ACS Nano* **2020**, *14*, 12621–12628.

[11] De Simoni, G.; Battisti, S.; Ligato, N.; Mercaldo, M. T.; Cuoco, M.; Giazotto, F. Gate control of the current-flux relation of a Josephson quantum interferometer based on proximitized metallic nanojuntions. *ACS Appl. Electron. Mater.* **2021**, *3*, 3927–3935.

[12] Paolucci, F.; Crisa, F.; De Simoni, G.; Bours, L.; Puglia, C.; Strambini, E.; Roddaro, S.; Giazotto, F. Electrostatic field-driven supercurrent suppression in ionic-gated metallic superconducting nanotransistors. *Nano Lett.* **2021**, *21*, 10309–10314.

[13] Ritter, M. F.; Fuhrer, A.; Haxell, D. Z.; Hart, S.; Gumann, P.; Riel, H.; Nichele, F. A superconducting switch actuated by injection of high-energy electrons. *Nat. Commun.* **2021**, *12*, 1266.

[14] Alegria, L. D.; Bøttcher, C. G. L.; Saydjari, A. K.; Pierce, A. T.; Lee, S. H.; Harvey, S. P.; Vool, U.; Yacoby, A. High-energy quasiparticle injection into mesoscopic superconductors. *Nat. Nanotechnol.* **2021**, *16*, 404–408.

[15] Golokolenov, I.; Guthrie, A.; Kafanov, S.; Pashkin, Y. A.; Tsepelin, V. On the origin of the controversial electrostatic field effect in superconductors. *Nat. Commun.* **2021**, *12*, 2747.

[16] Elalaily, T.; Kürtössy, O.; Scherübl, Z.; Berke, M.; Fülöp, G.; Lukács, I. E.; Kanne, T.; Nygård, J.; Watanabe, K.; Taniguchi, T. et al. Gate-controlled supercurrent in epitaxial Al/InAs nanowires. *Nano Lett.* **2021**, *21*, 9684–9690.

[17] Basset, J.; Stanisavljevic, O.; Kuzmanovic, M.; Gabelli, J.; Quay, C. H. L.; Estève, J.; Aprili, M. Gate-assisted phase fluctuations in all-metallic Josephson junctions. *Phys. Rev. Res.* **2021**, *3*, 043169.

[18] Orús, P.; Fomin, V. M.; De Teresa, J. M.; Córdoba, R. Critical current modulation induced by an electric field in superconducting tungsten-carbon nanowires. *Sci. Rep.* **2021**, *11*, 17698.

[19] Rocci, M.; Suri, D.; Kamra, A.; Vilela, G.; Takamura, Y.; Nemes, N. M.; Martinez, J. L.; Hernandez, M. G.; Moodera, J. S. Large enhancement of critical current in superconducting devices by gate voltage. *Nano Lett.* **2021**, *21*, 216–221.

[20] Ritter, M. F.; Crescini, N.; Haxell, D. Z.; Hinderling, M.; Riel, H.; Bruder, C.; Fuhrer, A.; Nichele, F. Out-of-equilibrium phonons in gated superconducting switches. *Nat. Electron.* **2022**, *5*, 71–77.

[21] Catto, G.; Liu, W.; Kundu, S.; Lahtinen, V.; Vesterinen, V.; Möttönen, M. Microwave response of a metallic superconductor subject to a high-voltage gate electrode. *Sci. Rep.* **2022**, *12*, 6822.

[22] Elalaily, T.; Berke, M.; Kedves, M.; Fülöp, G.; Scherübl, Z.; Kanne, T.; Nygård, J.; Makk, P.; Csonka, S. Signatures of gate-driven out-of-equilibrium superconductivity in Ta/InAs nanowires. *ACS Nano* **2023**, *17*, 5528–5535.

[23] Ruf, L.; Elalaily, T.; Puglia, C.; Ivanov, Y. P.; Joint, F.; Berke, M.; Iorio, A.; Makk, P.; De Simoni, G.; Gasparinetti, S. et al. Effects of fabrication routes and material parameters on the control of superconducting currents by gate voltage. *APL Mater.* **2023**, *11*, 091113.

[24] Yu, S.; Chen, L.; Pan, Y.; Wang, Y.; Zhang, D.; Wu, G.; Fan, X.; Liu, X.; Wu, L.; Zhang, L. et al. Gate-tunable critical current of the three-dimensional niobium nanobridge Josephson junction. *Nano Lett.* **2023**, *23*, 8043.

[25] Ruf, L.; Puglia, C.; Elalaily, T.; De Simoni, G.; Joint, F.; Berke, M.; Koch, J.; Iorio, A.; Khorshidian, S.; Makk, P. et al. Gate-control of superconducting current: Mechanisms, parameters and technological potential. *arXiv:* **2302**, *13734*, 2023.

[26] Fowler, R. H.; Nordheim, L. Electron emission in intense electric fields. *Proc. Roy. Soc. A* **1928**, *119*, 173–181.

[27] Mercaldo, M. T.; Solinas, P.; Giazotto, F.; Cuoco, M. Electrically tunable superconductivity through surface orbital polarization. *Phys. Rev. Appl.* **2020**, *14*, 034041.

[28] Mercaldo, M. T.; Giazotto, F.; Cuoco, M. Spectroscopic signatures of gate-controlled superconducting phases. *Phys. Rev. Res.* **2021**, *3*, 043042.

[29] Amoretti, A.; Brattan, D. K.; Magnoli, N.; Martinoia, L.; Matthaiakakis, I.; Solinas, P. Destroying superconductivity in thin films with an electric field. *Phys. Rev. Res.* **2022**, *4*, 033211.

[30] Chakraborty, S.; Nikolić, D.; Cuevas, J. C.; Giazotto, F.; Di Bernardo, A.; Scheer, E.; Cuoco, M.; Belzig, W. Microscopic theory of supercurrent suppression by gate-controlled surface depairing. *Phys. Rev. B* **2023**, *108*, 184508.

[31] Chen, W.; Rylyakov, A. V.; Patel, V.; Lukens, J. E.; Likharev, K. K. Rapid single flux quantum T-flip flop operating up to 770 GHz. *IEEE Trans. Appl. Supercond.* **1999**, *9*, 3212–3215.

[32] Likharev, K. K.; Semenov, V. K. RSFQ logic/memory family: A

new Josephson-junction technology for sub-terahertz-clock-frequency digital systems. *IEEE Trans. Appl. Supercond.* **1991**, *1*, 3–28.

[33] Kursun, V.; Friedman, E. G. *Multi-Voltage CMOS Circuit Design*; John Wiley & Sons, Ltd.: Chichester, 2006.

[34] Kaeslin, H. *Digital Integrated Circuit Design: From VLSI Architectures to CMOS Fabrication*; Cambridge University Press: Cambridge, 2008.

[35] Zikiy, E. V.; Ivanov, A. I.; Smirnov, N. S.; Moskalev, D. O.; Polozov, V. I.; Matanin, A. R.; Malevannaya, E. I.; Echeistov, V. V.; Konstantinova, T. G.; Rodionov, I. A. High-Q trenched aluminum coplanar resonators with an ultrasonic edge microcutting for superconducting quantum devices. *Sci. Rep.* **2023**, *13*, 15536.

[36] Cirillo, C.; Caputo, M.; Divitini, G.; Robinson, J. W. A.; Attanasio, C. Polycrystalline NbRe superconducting films deposited by direct current magnetron sputtering. *Thin Solid Films* **2022**, *758*, 139450.

[37] Cirillo, C.; Fittipaldi, R.; Smidman, M.; Carapella, G.; Attanasio, C.; Vecchione, A.; Singh, R. P.; Lees, M. R.; Balakrishnan, G.; Cuoco, M. Evidence of double-gap superconductivity in noncentrosymmetric $Nb_{0.18}Re_{0.82}$ single crystals. *Phys. Rev. B* **2015**, *91*, 134508.

[38] Smidman, M.; Salamon, M. B.; Yuan, H. Q.; Agterberg, D. F. Superconductivity and spin-orbit coupling in non-centrosymmetric materials: A review. *Rep. Prog. Phys.* **2017**, *80*, 036501.

[39] Cirillo, C.; Carapella, G.; Salvato, M.; Arpaia, R.; Caputo, M.; Attanasio, C. Superconducting properties of noncentrosymmetric $Nb_{0.18}Re_{0.82}$ thin films probed by transport and tunneling experiments. *Phys. Rev. B* **2016**, *94*, 104512.

[40] Scherrer, P. Bestimmung der Grösse und der inneren Struktur von Kolloidteilchen mittels Röntgenstrahlen. *Nachr. Ges. Wiss. Göttingen, Math. Phys. Kl.* **1918**, *1918*, 98–100.

[41] Likharev, K. K. Superconducting weak links. *Rev. Mod. Phys.* **1979**, *51*, 101–159.

[42] Karki, A. B.; Xiong, Y. M.; Haldolaarachchige, N.; Stadler, S.; Vekhter, I.; Adams, P. W.; Young, D. P.; Phelan, W. A.; Chan, J. Y. Physical properties of the noncentrosymmetric superconductor $Nb_{0.18}Re_{0.82}$. *Phys. Rev. B* **2011**, *83*, 144525.

[43] Nigro, A.; Nobile, G.; Rubino, M. G.; Vaglio, R. Electrical resistivity of polycrystalline niobium nitride films. *Phys. Rev. B* **1988**, *37*, 3970–3972.

[44] Marsili, F.; Gaggero, A.; Li, L. H.; Surrente, A.; Leoni, R.; Lévy, F.; Fiore, A. High quality superconducting NbN thin films on GaAs. *Supercond. Sci. Technol.* **2009**, *22*, 095013.

[45] Colton, R. Technetium chlorides. *Nature* **1962**, *193*, 872–873.

[46] Woolf, A. A. An outline of rhenium chemistry. *Q. Rev. Chem. Soc.* **1961**, *15*, 372–391.

[47] Brown, D.; Colton, R. 141. The magnetic properties of rhenium halides. Part I. Rhenium tetra-, penta-, and hexa-chloride. *J. Chem. Soc.* **1964**, *8*, 714–717

[48] Knox, K.; Coffey, C. E. Chemistry of rhenium and technetium. II. Magnetic susceptibilities of $ReCl_5$, $ReCl_3$, $TcCl_4$ and $MoCl_5$. *J. Am. Chem. Soc.* **1959**, *81*, 5–7.